International Journal of Fatigue 62 (2014) 180–193

Contents lists available at SciVerse ScienceDirect

International Journal of Fatigue

journal homepage: www.elsevier.com/locate/ijfatigue

Micro-mechanical modelling of fretting fatigue crack initiation and wear in Ti–6Al–4V

O.J. McCarthy, J.P. McGarry, S.B. Leen *

Mechanical and Biomedical Engineering, NUI Galway, Ireland

ARTICLE INFO

Article history:
Received 24 October 2012
Received in revised form 23 January 2013
Accepted 22 April 2013
Available online 2 May 2013

Keywords:
Fretting wear
Crystal plasticity
Ti–6Al–4V
Crack nucleation

ABSTRACT

A micro-mechanical modelling methodology is presented for predicting fretting fatigue crack nucleation in Ti–6Al–4V. The methodology is based on a combination of (i) a unit cell crystal plasticity model of Ti–6Al–4V, (ii) a frictional contact model of an experimental fretting wear configuration, and (iii) implementation of a microstructure-sensitive fatigue indication parameter for prediction of crack nucleation. A novel micro-mechanical method for wear prediction is presented. A key finding is the important role of cyclic micro-plasticity in ostensibly elastic loading regimes in fretting wear, resulting in significant effects on distributions of salient fretting contact variables such as contact pressure.

1. Introduction

Fretting is a phenomenon that takes place when two materials come into contact under a normal load and are subjected to a cyclic tangential force which results in displacements typically in the range of 5–100 μm. It can occur in a wide range of industries, typically aerospace, biomedical and offshore oil and gas. A large number of parameters are responsible for fretting fatigue such as normal load, tangential force, coefficient of friction (COF), surface roughness and micro-mechanical properties. This results in fretting damage being a complex problem making component life difficult to predict. This phenomenon normally results in two main sliding regimes (i) partial slip and (ii) gross sliding. When a tangential force is applied to one of the contacting bodies the relative displacement between the two bodies increases until a stick region is present in the centre. This sliding regime is more commonly referred to as partial slip and results in localised stress concentrations at the stick-slip interface. This slip regime commonly results in crack initiation and premature part failure. When the tangential force increases further and overcomes the surface shear traction gross sliding is achieved. This sliding regime normally results in large amounts of material removal as a result of micro-cracking (e.g. asperities) and wear. This leads to a more uniform distribution of micro damage across the entire contact zone and results in a longer fatigue life compared with the partial slip regime.

Fretting maps, as seen in [1], show the relationship between contact pressure and displacement amplitude for each sliding regime. Vingsbo and Soderberg [2] describe the effect of sliding regime on component life. A significant increase in part life is evident as slip amplitude is increased from the partial slip regime to the gross slip regime. It is also evident that the modelling of material removal is necessary for accurate gross slip life predictions. This importance is highlighted by Madge et al. [3,4] where the effect of slip amplitude and consequently slip regime was investigated for Ti–6Al–4V. This was achieved by implementing a material removal simulation tool based on the Archard equation [5]. The Archard equation is a commonly-used wear law which has been shown to successfully predict sliding wear across a wide range of materials and loading conditions [6]. Life predictions were based on the Smith–Watson–Topper (SWT) fatigue indication parameter (FIP), corresponding to macroscopic crack lengths (e.g. 1 mm long cracks). This does not distinguish between different cracking regimes, as shown by the following equation:

$$N_f = N_i + N_{MSC} + N_{PSC} + N_{LC} \quad (1)$$

where N_f is the total life predictions, N_i is the number of cycles to crack nucleation, N_{MSC} is microstructurally short crack growth, N_{PSC} is physically short crack growth and N_{LC} is long crack growth as described by McDowell and Dunne [7].

Previous work carried out by Ding et al. [8] has presented a modified macroscopic FIP method to predict crack nucleation lives for Ti–6Al–4V, compared with experimentally obtained data. Fretting tests were carried out under a variety of loading conditions which resulted in different slip regimes and crack nucleation lives. Crack location, angle and life were predicted using a critical plane SWT approach in combination with a wear simulation tool and Miner's rule. This approach used back-calculated fatigue constants,

* Corresponding author. Tel.: +353 (0) 91 495955; fax: +353 (0)91 563991.
E-mail address: sean.leen@nuigalway.ie (S.B. Leen).

0142-1123/$ - see front matter © 2013 Elsevier Ltd. All rights reserved.
http://dx.doi.org/10.1016/j.ijfatigue.2013.04.019

Nomenclature

N_f	total number of cycles to failure
N_i	number of cycles to crack initiation
N_{MSC}	number of microstructurally short crack growth cycles
N_{PSC}	number of physically short crack growth cycles
N_{LC}	number of long crack growth cycles
α	slip system
β	slip system not equal to α
$\dot{\gamma}^{\alpha}$	shear strain rate on slip system α
$\dot{\alpha}$	reference strain rate
τ^{α}	resolved shear stress on slip system α
g^{α}	strain hardness on slip system α
m	rate sensitivity exponent
$h_{\alpha\beta}$	strain hardening modulus
g_0	critical resolved shear stress
g_{∞}	saturation stress
h_0	initial hardening modulus
γ_{α}	accumulated shear strain
α phase	HCP structure
α–β phase	HCP–BCC structure
p	accumulated plastic slip
$\boldsymbol{L}^p$	plastic velocity gradient
$\dot{p}$	effective plastic slip rate
$\boldsymbol{s}^{\alpha}$	slip direction vector
$\boldsymbol{n}^{\alpha}$	slip normal vector
p_{crit}	critical accumulated plastic slip
p_{cyc}	accumulated plastic slip per cycle
P	normal load
$\Delta\varepsilon_p$	plastic strain range
ε'_f	fatigue ductility coefficient
c	fatigue ductility exponent
N_p	number of cycles to crack propagation
δ_{app}	cyclic displacement
P_y	normal load required to cause yielding
R	pad radius
E^*	composite modulus
Y	yield stress
ν	Poisson's ratio
E	Young's modulus
N	number of FE cycles
x_i	horizontal location
d_i	depth
$p(x)$	contact pressure as a function of x-position
k	wear coefficient
V	wear volume
S	total sliding distance
a_0	initial contact semi-width

Abbreviations

COF	coefficient of friction
SWT	Smith Watson Topper
FIP	fatigue indicator parameter
CP	crystal plasticity
SS	stainless steel
HCP	hexagonal close packed
BCC	body centred cubic
CSSC	cyclic stress–stain curve
LCF	low cycle fatigue
HCF	high cycle fatigue
UMAT	user material subroutine
NLKH	non-linear kinematic hardening

corresponding to 10 μm crack lengths, via an El-Haddad short crack growth method, as presented by Madge et al. [9]. Crack lengths, typically of the same size as metallic grains (20–50 μm), were observed experimentally by Ding et al. [8], among others, for Ti–6Al–4V and other metallic materials in fretting. A physically-based finite element (FE) model is required for scale consistency in such situations, where modelling of individual grains, orientations and slip systems is necessary. For this reason a crystal plasticity (CP) material model is implemented here for more scale consistent predictions of crack nucleation. CP theory models crystallographic slip on individual slip systems within metallic grains. CP has been used to study the effects of microstructure, such as orientation, texture and grain size on numerous complex loading situations. This rate-dependant theory has been used extensively in the design of stent struts by McHugh and Connolly [10] and McGarry et al. [11] for 316L stainless steel (SS). CP has been used by McDowell and co-workers [12–14] to model fretting of Ti–6Al–4V.

Most FIP's predict total life (N_f) and do not have the ability to separate crack initiation life from crack propagation life. A methodology previously implemented by Manonukul and Dunne [15] has shown success with regards to predicting the crack initiation life for nickel C263 for low and high cycle fatigue. McCarthy et al. [16] predicted crack initiation lives, but without any experimental validation or comparison for the fretting predictions, for 316L SS in plain fatigue and in a cylinder-on-flat fretting configuration. This methodology is based on the identification of a critical accumulated crystallographic plastic slip parameter that denotes when crack initiation has occurred. It is a microstructure-sensitive methodology, that is dependent on microstructural features such as crystallographic orientation, texture and grain size.

Ti–6Al–4V is an important material for a range of applications due to its low weight, high strength, excellent corrosion resistance and biocompatibility. However it is well known to be susceptible to fretting wear and fatigue failure. A key fundamental issue for design against fretting is the prediction of crack nucleation. Due to the versatility and widespread use of titanium alloys, a significant amount of work has been carried out on characterising its failure behaviour. The complex microstructure of Ti–6Al–4V is comprised of a dual phase structure containing both hexagonal close packed (HCP) and body centre cubic (BCC) crystals; the α phase has a HCP crystallographic arrangement and the α–β phase is comprised of a lamellar colony of both HCP and BCC crystallographic arrangements. Extensive modelling of Ti–6Al–4V microstructure has been carried out by McDowell [12–14] and Cailletuad [17,18]. Benedetti and Fontanari [19] established monotonic and cyclic stress strain curves (CSSCs) for Ti–6Al–4V while investigating fatigue crack growth. Hasija et al. [20] investigated the cold creep phenomenon of Ti–6Al alloy using a variety of strain rates under monotonic loading. Both sets of experimental data are used here for calibration of the material model.

2. Methodology

2.1. Crystal plasticity theory

The crystal plasticity theory [21] used in this paper is a physically-based, rate-dependant crystallographic theory that models the deformation of a metallic crystal lattice. Plastic slip is assumed to obey Schmidt's law [21], where the rate of plastic shear strain, $\dot{\gamma}^{\alpha}$, for a particular slip system, α, is assumed to depend on the resolved shear stress, τ^{α}, through the following power law:

$$\dot{\gamma}^{\alpha} = \dot{a}\ \mathrm{sgn}(\tau^{\alpha})\left\{\left|\frac{\tau^{\alpha}}{g^{\alpha}}\right|\right\}^{m} \tag{2}$$

where $\dot{a}$ and m are the reference strain rate and rate sensitivity exponent, respectively. Material strain hardening on slip system α, is specified by the slip system strain hardness, g^{α}, which is defined by the integral of the following equation:

$$\dot{g}^{\alpha} = \sum_{\beta} h_{\alpha\beta}\dot{\gamma}^{\beta} \tag{3}$$

where $h_{\alpha\beta}$ is the strain hardness moduli and α and β represent particular slip systems. When $\alpha = \beta$, this parameter represents self hardening moduli and $\alpha \neq \beta$, it represents latent hardening moduli. In this work Taylor isotropic hardening is assumed and self and latent hardening moduli are considered equal. $g(\gamma_{\alpha})$ is the slip system strain hardness defined by the following hardness function [22]:

$$g(\gamma_a) = g_0 + (g_{\infty} - g_0)\ \tanh\left|\frac{h_0\gamma_a}{(g_{\infty} - g_0)}\right| \tag{4}$$

where h_0 is the initial hardening modulus, g_{∞} is the saturation stress and g_0 is the critical resolved shear stress. The hardening moduli can be found through differentiation of the above equation, as follows:

$$h_{\alpha\beta} = h(\gamma) = h_0\ \mathrm{sech}^2\left|\frac{h_0\gamma_a}{(g_{\infty} - g_0)}\right| \tag{5}$$

The accumulated slip, γ_{α} is defined as follows:

$$\gamma_a = \sum_{\alpha}\int_0^t |\dot{\gamma}^{\alpha}|dt \tag{6}$$

This theory is implemented here in Abaqus 6.10 via a user defined material, (UMAT) user subroutine following the approach of [22]. Further details are given in [16].

2.2. Micro mechanical model

Ti–6Al–4V consists of a dual phase microstructure, typically divided into 60% α phase and 40% α–β phase. α phase consists of normal HCP crystalline structure with plastic slip occurring on the basal $3\langle 11\bar{2}0\rangle\{0001\}$, prismatic $3\langle 11\bar{2}0\rangle 10\bar{1}0$ and pyramidal $3\langle 11\bar{2}0\rangle 10\bar{1}1$ slip systems as seen in Fig. 1. Due to the high resolved shear stress required for slip to occur on the pyramidal plane, three times that of the basal plane [23], pyramidal slip is not modelled in this work. The lamellar structure of the α–β phase is modelled by combining both HCP and BCC slip systems into a continuous homogeneous phase [24]. This phase is not modelled as individual alternating layers of α and β due to the small size scales of these layers. This would significantly increase mesh density and result in potentially detrimental computational overhead; instead, following the approach of [12], a continuous grain with representative properties is implemented. This consists of 12 BCC slip systems $\langle 111\rangle\{110\}$ and the previously mentioned HCP slip systems together. Twinning is also neglected here for Ti–6Al–4V, based on the work of Dick and Cailletaud [17] and Morrissey et al. [24].

2.3. Microstructure-sensitive crack initiation methodology

A microstructure-sensitive prediction methodology previously developed by Manonukul and Dunne [15] is implemented. It is proposed that there exists a microstructural parameter, accumulated plastic slip, p, that is the controlling factor for crack initiation. p is defined by the following equations:

$$\dot{p} = \left(\frac{2}{3}\boldsymbol{L}^p : \boldsymbol{L}^p\right)^{\frac{1}{2}} \quad p = \int_0^t \dot{p}dt \tag{7}$$

where the plastic velocity gradient $\boldsymbol{L}^p$ is defined by:

$$\boldsymbol{L}^p = \sum_{\alpha=1}^{n}\dot{\gamma}\boldsymbol{s}^{\alpha}\boldsymbol{n}^{\alpha^T} \tag{8}$$

with $\boldsymbol{s}^{\alpha}$ and $\boldsymbol{n}^{\alpha}$ as the slip direction and normal vectors, respectively, for a given slip system, α, with n slip systems. $\dot{p}$ and p are coupled in the CP user subroutine. Crack initiation is deemed to have occurred once p has reached a critical value of accumulated plastic slip, p_{crit}. This critical value is calculated using an experimentally determined number of cycles to initiation, N_i, and the maximum (with respect to location) accumulated plastic slip in one cycle, p_{cyc}, for the same loading conditions. Due to the predicted rapid stabilisation of p with respect to the number of fatigue cycles, N, it is possible to determine p_{crit} from the following:

$$p_{crit} = N_i p_{cyc} \tag{9}$$

The measured experimental low cycle fatigue (LCF) response of the material is encapsulated by the Coffin–Manson relationship between predicted number of cycles to failure (initiation), N_i, and plastic strain range, $\Delta\varepsilon_p$, as follows:

$$N_i = \left(\frac{\Delta\varepsilon_p}{\varepsilon_f'}\right)^{\frac{1}{c}} \tag{10}$$

where ε_f' and c are material constants given in Table 1. The p_{crit} value for Ti–6Al–4V is identified using the N_i value corresponding to one particular value of plastic strain range, $\Delta\varepsilon_p$. Short crack growth estimations, based on the El Haddad approximation and Paris crack

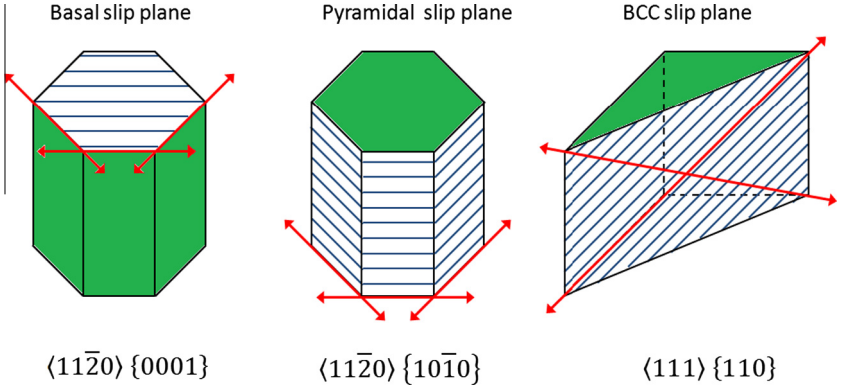

Fig. 1. Simple schematic of the crystallographic slip systems for α and α–β phase, where the red arrows represent the slip directions and the hatched lines represent the slip planes.

Table 1
Fatigue constants for Coffin–Manson equation for Ti–6Al–4V [3].

ε_f'	0.841
c	−0.688

Table 2
Loading parameters for experimental fretting tests [6].

Regime	Normal load (N/mm)	Stroke (μm)
Gross slip	50	80
Partial slip	100	50

growth, for the lower load levels of relevance to the LCF life range, indicate that the numbers of cycles for crack propagation, N_p, are less than 10% of N_f. Hence it is assumed here, for uniaxial plain fatigue loading, that $N_i \approx N_f$ as obtained from the Coffin–Manson data.

2.4. Cylinder on flat contact model

An FE cylinder-on-flat fretting configuration based on the experimental work of Ding et al. [8] is implemented within this paper. The loading conditions used within the FE fretting model are tabulated in Table 2, including the applied parameters and resulting slip regimes. The simple schematic of Fig. 2 illustrates the experimental arrangement. The cylindrical specimen is in contact with the flat specimen under the action of a normal load, P, and is subjected to a controlled cyclic tangential displacement or stroke, δ_{app}. The flat specimen is not subjected to an applied bulk fatigue load. It is argued that the added complication of such a bulk fatigue load is unnecessary in terms of identifying and understanding crack nucleation. This experimental arrangement has been successfully implemented in work such as McColl et al. [25] for high strength aero-engine steel, to characterise the fretting behaviour under different normal loads and strokes.

The FE model follows the approach adopted in previous work by McCarthy et al. [16] and McColl et al. [25]. A two-dimensional plane strain FE model as seen in Fig. 3 is developed with a 6 mm cylindrical pad in contact with a 5 × 10 mm substrate. Numerous authors have reported a COF for Ti–6Al–4V under fretting conditions. The current work is based on experimental observations by Ding et al. [8] where a COF of 0.9 is reported for gross sliding conditions. Furthermore, experimental work carried out by Jin and Mall [26] for fretting on Ti–6Al–4V have reported a similar COF value in the region of 1.1 for the same sliding regime. The region of contact is of greatest interest within this work; therefore the greatest mesh density is used in this area, giving a minimum element size of 2.5 μm. Within the fretting model uniform square grains are used. This facilitates better mesh control and more systematic analysis of results. A previous comparison study between square and hexagonal grains [16] showed almost identical results in terms of p. The square grain microstructure implemented here also includes triple points. It is important to note that the two-dimensional geometry used throughout this work is an approximation of a three-dimensional microstructure. However, each grain is assigned a unique three-dimensionally oriented crystallographic structure (specified at the integration points within the UMAT), which captures, to some extent, the three-dimensional nature of the microstructure. The three-dimensional CP modelling of a microstructure has been reported to be computationally demanding, e.g. see [11], for tensile testing of stent struts. Comparisons between the current two-dimensional approach and full three-dimensional analyses in [11] showed that the run-times for the latter were about fifty times those of the former. With the added complexity of a cyclic frictional contact problem, one can expect further significant increases in computational time. Nevertheless, some previous authors (Dick and Cailletaud [17] and Zhang et al. [13]) have modelled fretting problems using three-dimensional CP. One concern with two-dimensional CP modelling is that it misrepresents the number of grains present within a problem, so that grain orientation has a significant effect on results. To address this here, a random orientation study is presented (see below).

Two different material models are used here, namely a J_2 nonlinear kinematic hardening (NLKH) model and a crystal plasticity material model. There are also two fretting models. The first is a hybrid model (see Fig. 3), with a CP region positioned in the area of interest, the contact region, surrounded by a J_2 NLKH model. Within this CP region there are 210 square grains, 30 × 7, consisting of an element size of 2.5 μm; each grain is assigned a unique randomly generated grain orientation, in addition to a randomly assigned material phase. The second is a J_2 fretting model, which uses the J_2 NLKH material model for both contacting surfaces, i.e. the substrate specimen and the cylindrical pad. The material constants are listed in Table 3, taken from Benedetti and Fontanari [19]. Compliance within the experimental rig, with respect to tangential force–displacement response, is modelled here using a horizontal spring element as shown in Fig. 3. Fig. 4 shows the comparison of the FE and measured tangential force displacement response for the calibrated spring stiffness.

As previously mentioned, normal load has a significant effect on fretting. Using Hertzian contact mechanics [27] the normal load required to cause yielding is as follows:

$$P_y = \frac{\pi R}{E^*}(p_0)_Y^2 \tag{11}$$

where

$$1.8Y = (p_0)_Y \tag{12}$$

where R is the radius of the pad, Y is the yield stress of the material and E^* is the composite modulus defined by the following:

$$\frac{1}{E^*} = \frac{1-\nu_1^2}{E_1} + \frac{1-\nu_2^2}{E_2} \tag{13}$$

where ν and E are Poisson's ratio and Young's modulus of each material respectively. The largest normal load applied within this work is 100 N/mm, which is equal to $0.15P_y$, i.e. well within the nominally elastic regime.

2.5. Microstructure-sensitive fretting damage

The significant difference between partial and gross slip and the resulting surface damage has been previously mentioned. It is important particularly in the context of micro-crack nucleation, due to contact stresses, to develop a method for distinguishing between fretting wear and cracking. Fig. 5 introduces two different damage concepts via a simple schematic. Case A (cracking) shows localised discrete areas where large concentrations of accumulated crystallographic slip, p, greater than p_{crit} have developed. Case A represents a typical partial slip situation with cracking concentrated in the slip zones. Case B (wear) illustrates a simply connected, more evenly distributed region of accumulated crystallographic slip, p, greater than the critical value, p_{crit}. It is important to note here that Sweeney et al. [28], for example, have shown that cyclic micro-plasticity occurs in situations where loading is ostensibly elastic (at a macro scale). This distributed micro-cracking process, effectively wear, is characteristic of gross slip situations where micro-damage occurs throughout the entire contact region. The stabilised accumulated plastic slip per cycle parameter,

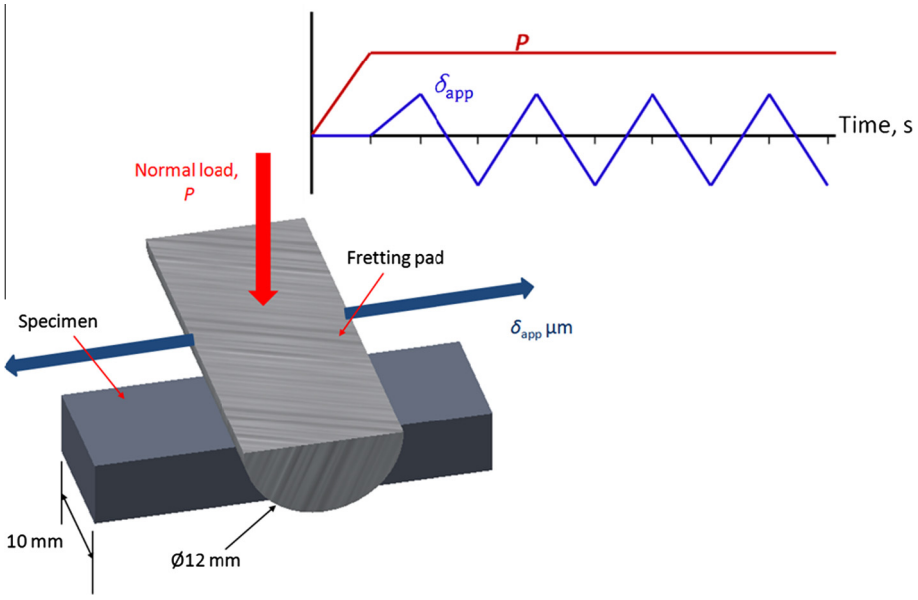

Fig. 2. Simple fretting test schematic plus the load and displacement history of the experimental arrangement.

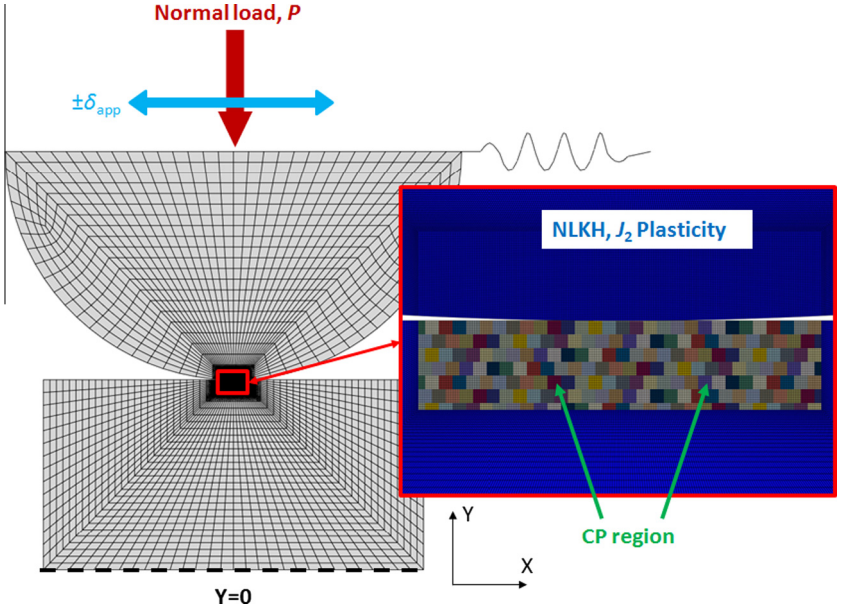

Fig. 3. FE frictional contact model highlighting the CP region in the contact zone.

p_{cyc}, is implemented here, within a numerical methodology to predict wear depth, based on the assumption that any material with $p(x, y, N) \geqslant p_{crit}$ has been worn away after that number of fretting cycles, N. Fig. 6 illustrates the process, as follows:

1. Firstly, distributions of p versus depth (at integration points) are computed for different horizontal locations x_i across the contact width, by assuming that the stabilised (integration point) values of accumulated plastic slip, $p_{cyc}(x,y)$, from early fretting cycles, can be extrapolated to large numbers of fretting cycles, using the equation $p(x,y,N) = p_{cyc}(x,y)N$.
2. For a given p_{crit}, corresponding to micro-crack initiation, it is then possible to identify, by interpolation with respect to integration point values of $p(x,y,N)$, for each value of x_i, the depth d_i to which $p(x, y, N) \geqslant p_{crit}$ after a given number of cycles, N. This distribution of depth $d_i(x_i,N)$ is then taken as the predicted wear depth distribution for that number of cycles N.

Hence, the methodology provides wear depth distributions for different numbers of fretting cycles.

3. Results

3.1. Crystal plasticity calibration process

Two different CP models are investigated:

Table 3
Material data, including non-linear kinematic hardening data, for Ti–6Al–4V [19].

E	116 GPa
ν	0.342
k	840 MPa
C	8976 MPa
γ	102

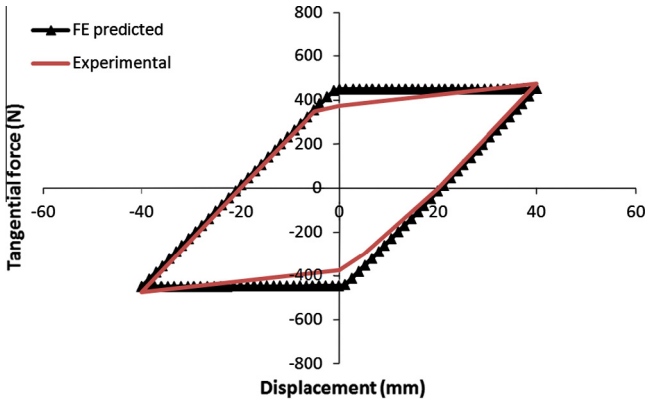

Fig. 4. Comparison between the measured [8] and FE predicted tangential force displacement hysteresis loops.

- A single-phase CP model, where one set of CP hardening constants is used to represent both the α phase and the α–β phases.
- A dual-phase CP model, where two sets of hardening constants are used to separately model the α phase and the α–β phase.

A unit cell model consisting of a uniform hexagonal grain morphology is implemented, as shown in Fig. 7, for calibration of the CP material and failure constants. The hexagonal morphology includes triple points which are an important feature in microstructural modelling and deformation. Individual random crystallographic orientations are assigned to each grain. A random number generator is used to arbitrarily assign grains as either α or α–β phase throughout the dual-phase model in the correct volume fraction proportions. The unit cell consists of 42 uniform size hexagonal grains and 22 partial grains making up the grain boundaries. 4200 four-noded, plane strain elements and symmetry boundary conditions are used; more details are given in [16]. A grain size of 20 μm is used for both phases based on the micrographs of Ding et al. [8].

Individual CP material parameters (h_0, g_∞, g_0), as per Eq. (5), are calibrated for each phase. This was achieved by identifying the CP parameters for the α phase via an iterative calibration process using α-phase Ti–6Al monotonic tensile data at different strain rates [20], as seen in Fig. 8. In this case the CP unit cell model was comprised entirely of α phase grains. Benedetti [19] provides cyclic stress–strain curves (CSSCs) for Ti–6Al–4V. Keeping the identified α phase CP parameters (see Table 4), the dual phase unit cell model (composed of randomly generated α-phase and α–β phase grains) is subjected to uniaxial strain-controlled, fatigue loading and compared to the CSSC for Ti–6Al–4V, to iteratively identify the CP material constants for the α–β phase. In the case of the single phase CP model, the CSSC data for Ti–6Al–4V [19] was sufficient to calibrate the single set of hardening constants. Table 4 tabulates the CP hardening constants for both phases in the dual phase model and the single phase model. The effect of random orientation on the cyclic stress strain response is also investigated for the dual phase CP model. Five different random orientation sets are assigned to the microstructure and the results of the calibration process for the dual phase are presented in Fig. 9, which compares the experimental results [19] and the FE predictions corresponding to the identified dual phase material constants.

3.2. Predicted low cycle behaviour of Ti–6Al–4V

Using a single N_i value and corresponding plastic strain range, $\Delta\varepsilon_p$, a p_{crit} value of 126 is identified for micro-crack nucleation

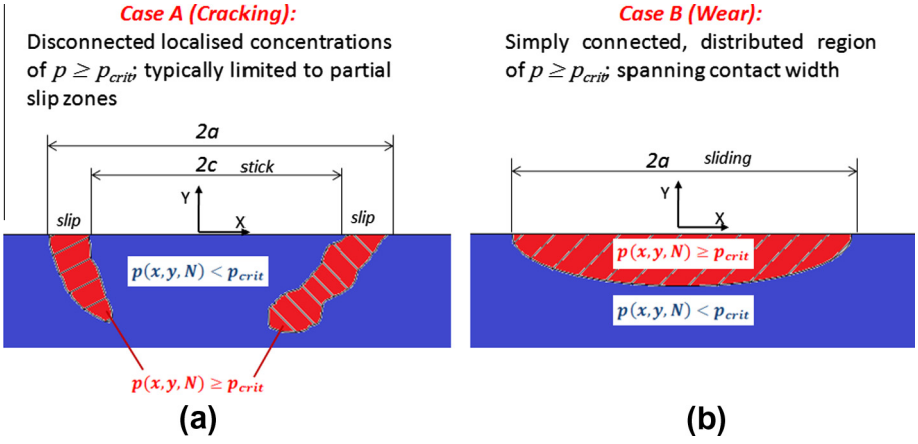

Fig. 5. Distributions of accumulated plastic slip greater than the critical value (a) partial slip (cracking) and (b) gross sliding (wear).

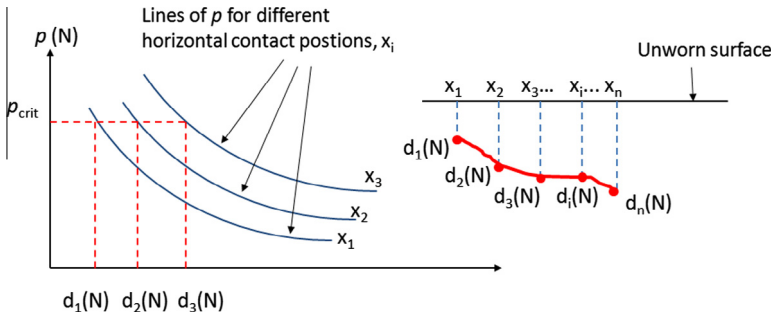

Fig. 6. Simple schematic of the microstructure-sensitive fretting wear predictive methodology for a given number of fretting cycles *N*.

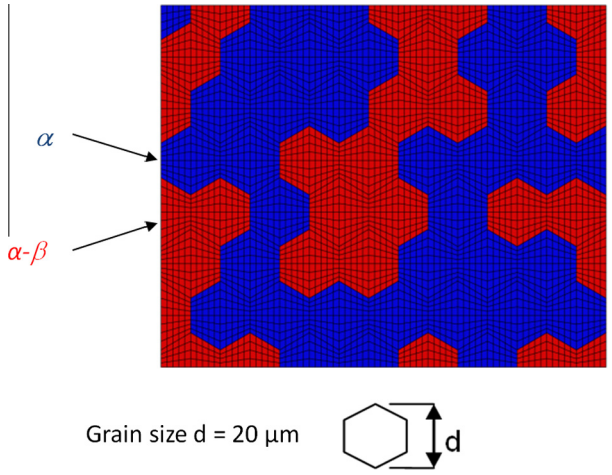

Fig. 7. Unit cell model highlighting the random distributions of α and α–β phases.

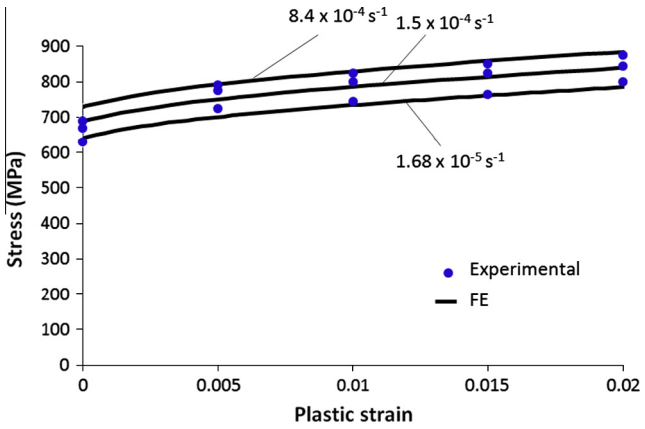

Fig. 8. Comparison between experimental [20] and FE monotonic uniaxial loading response for iteratively identified α phase constants of Table 4.

Table 4
Identified CP constitutive constants for cyclic behaviour of Ti–6Al–4V for both CP models.

	Single phase	Dual phase	
		α phase	α–β phase
h_0 (MPa)	170	220	128
g_∞ (MPa)	270	650	175
g_0 (MPa)	165	265	75
$\dot{a}$ (s^{-1})	0.0023	0.0023	0.0023
m	30	30	30

following the approach of [15] for the dual-phase CP model. Using this value of p_{crit} the entire LCF strain-life response of Ti–6Al–4V can be predicted. Fig. 10 shows the correlation between the Coffin–Manson equation and these microstructure-sensitive crack initiation predictions (CP response). The effect of random orientation on CP predicted life, as represented by the horizontal error bars, illustrates the ability of the CP model to represent fatigue life scatter due to microstructural inhomogeneity. This same methodology and identified p_{crit} value is subsequently applied to a dual-phase cylinder-on-flat fretting configuration, below, to predict micro-crack nucleation and wear. A similar method is applied to identify the single phase p_{crit} value.

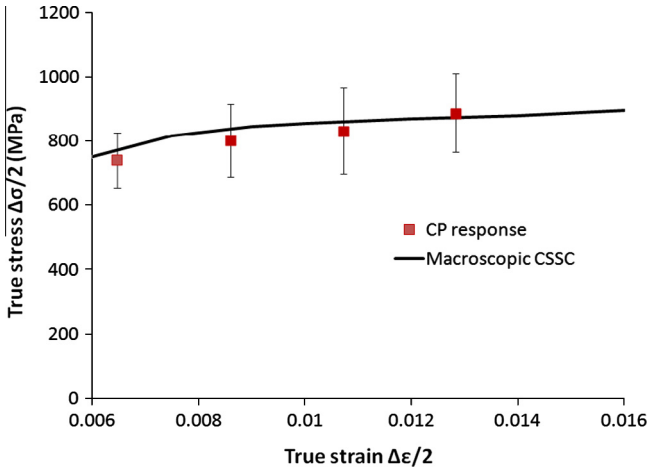

Fig. 9. Comparison between the CP cyclic response corresponding to identified dual phase material constants and the experimental cyclic stress–strain curve (CSSC) for Ti–6Al–4V [19]. The error bars correspond to the effect of different distributions of random crystallographic orientation on the predicted cyclic response.

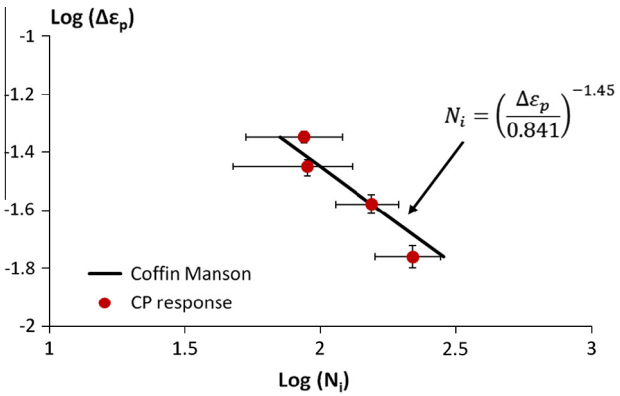

Fig. 10. Comparison of CP based life predictions compared to the Coffin–Manson relationship including the effect of random orientation.

3.3. Single-phase CP fretting analysis

Fig. 11 shows the predicted evolutions of partial slip contact variable distributions for the two different material models, J_2 and single phase CP. The contact variables are plotted as a function of x/a_0, where a_0 is the contact semi width for the initial normal load, $N = 0$. The contact pressure distributions for the J_2 model and the initial ($N = 0$) contact pressure for the CP model agree with the analytical (Hertzian) solution (Fig. 11a and b). However with increased fretting cycles it is clear that surface microstructural inhomogeneities lead to an inhomogeneous distribution of contact pressure. Goh et al. [14] described this as the development of a "natural surface roughness" in the contact wear scar. Hence, for $N > 1$ the mean CP pressure distribution follows the general Hertzian profile but with significant local variations about this mean Hertzian distribution, giving rise to locally (much) higher peak contact pressures. By $N = 6$, the distribution has effectively stabilised due to plastic shakedown. The characteristic partial slip surface shear distribution is evident from the J_2 model (Fig. 11c), where the central stick zone has a contact shear value less than $\mu p(x)$.The CP predicted shear stress distribution ($N = 1$) also shows significant microstructure induced variations (Fig. 11d) about the mean (J_2) partial slip distributions of Fig. 11c. The distribution has effectively stabilised by about $N = 12$ in Fig. 11d. In this case the local peaks are not predicted

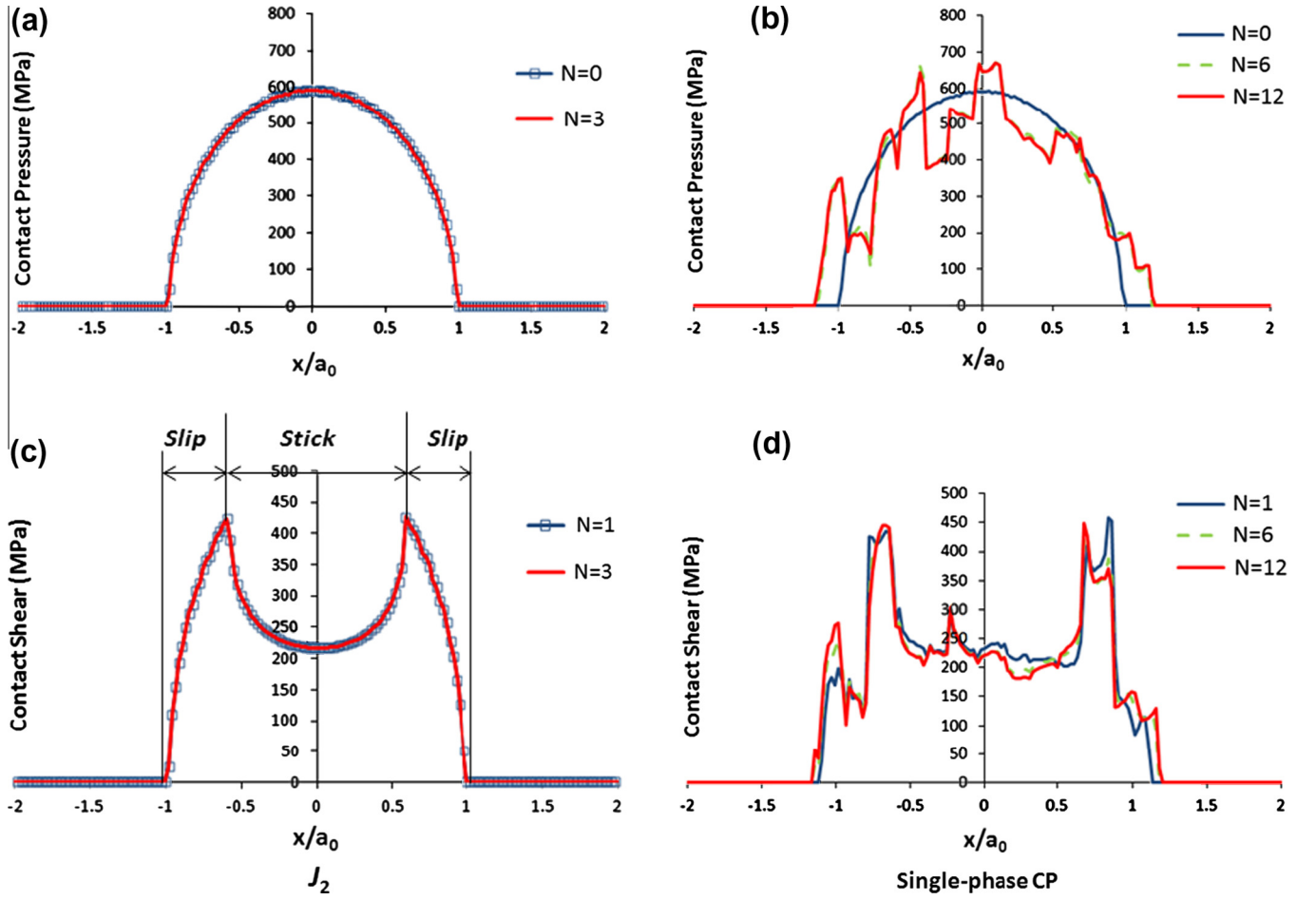

Fig. 11. Evolutions of contact variable distributions for J_2 and single phase CP model under partial slip conditions where P = 100 N/mm and δ_{app} = 80 μm, (a_0 = initial contact semi width).

to exceed the peak partial slip values at the stick–slip interface of Fig. 11c. Similar trends are predicted for gross slip loading conditions, as shown in Fig. 12. Comparison to the Hertzian solution shows good agreement for both the J_2 model and the initial $N = 0$ cycle for the single phase CP model. Clearly frictional effects (shear) have a significant effect in terms of micro-plasticity on the distributions of contact pressure and shear. Significant micro-plasticity is evident in the case of the single phase CP model even in this nominally elastic loading situation. A significant widening of the contact area (11–18%) is predicted by the CP model especially for the higher normal load (partial slip case) as a result of tangentially-induced (frictional) plastic deformation. Note that the contact pressure distributions are sampled at the zero-stroke position while the shear traction distribution is sampled at the extreme stroke position.

Fig. 13 shows the predicted distributions of accumulated crystallographic plastic slip per cycle, p_{cyc}, for the partial and gross slip cases. These distributions are calculated at the top layer of integration points on the substrate surface. For the partial slip case, Fig. 13a, highly localised concentrations of p_{cyc} are present in the slip zones with a zero p_{cyc} region in the stick zone. A more uniform distribution is predicted for the gross slip condition in Fig. 13b. It is proposed here that this more uniform distribution of p_{cyc} be treated as a multiple micro-cracking process which eventually leads to material removal (Case B). The predicted crack initiation lives, based on the microstructure-sensitive methodology, for both regimes are presented in Table 5.

3.4. Dual phase CP fretting crack initiation

The dual phase model is used to compare against the experimentally observed crack initiation lives, locations and orientations from the work presented by Ding et al. [8]. Using this more realistic representation of the microstructure, the contact variables are presented in Fig. 14, where a greater degree of inhomogeneity is evident in both the contact pressure and shear evolutions as compared to the single phase case. The peak surface tractions coincide with surface phase boundary locations. In the experimental fretting tests, cracks were observed at lengths ranging from 5 to 50 μm, after up to 10^5 cycles. Fig. 15 shows the effect of random grain orientations for a sample of orientation sets for contact pressure and shear. Clearly, microstructure is predicted to have a significant effect on these distributions, both qualitatively, in terms of local peaks in normal or shear traction (note again that the contact pressure distribution is sampled at the zero-stroke position, while the shear traction is sampled at the extreme stroke position), and quantitatively, in terms of magnitudes of instantaneous peak pressures and shears. Table 6 shows an average initiation life, of 5×10^3, which is consistent with the experimental observations. Microscopy techniques used in the experimental work quantified crack orientation and location. Comparisons are made in Table 6 between the predicted crack initiation lives of the different microstructures (random orientation sets). Fig. 16 shows an inhomogeneous distribution of contact slip, corresponding with the distributions of contact pressure and shear of Fig. 11, which, as

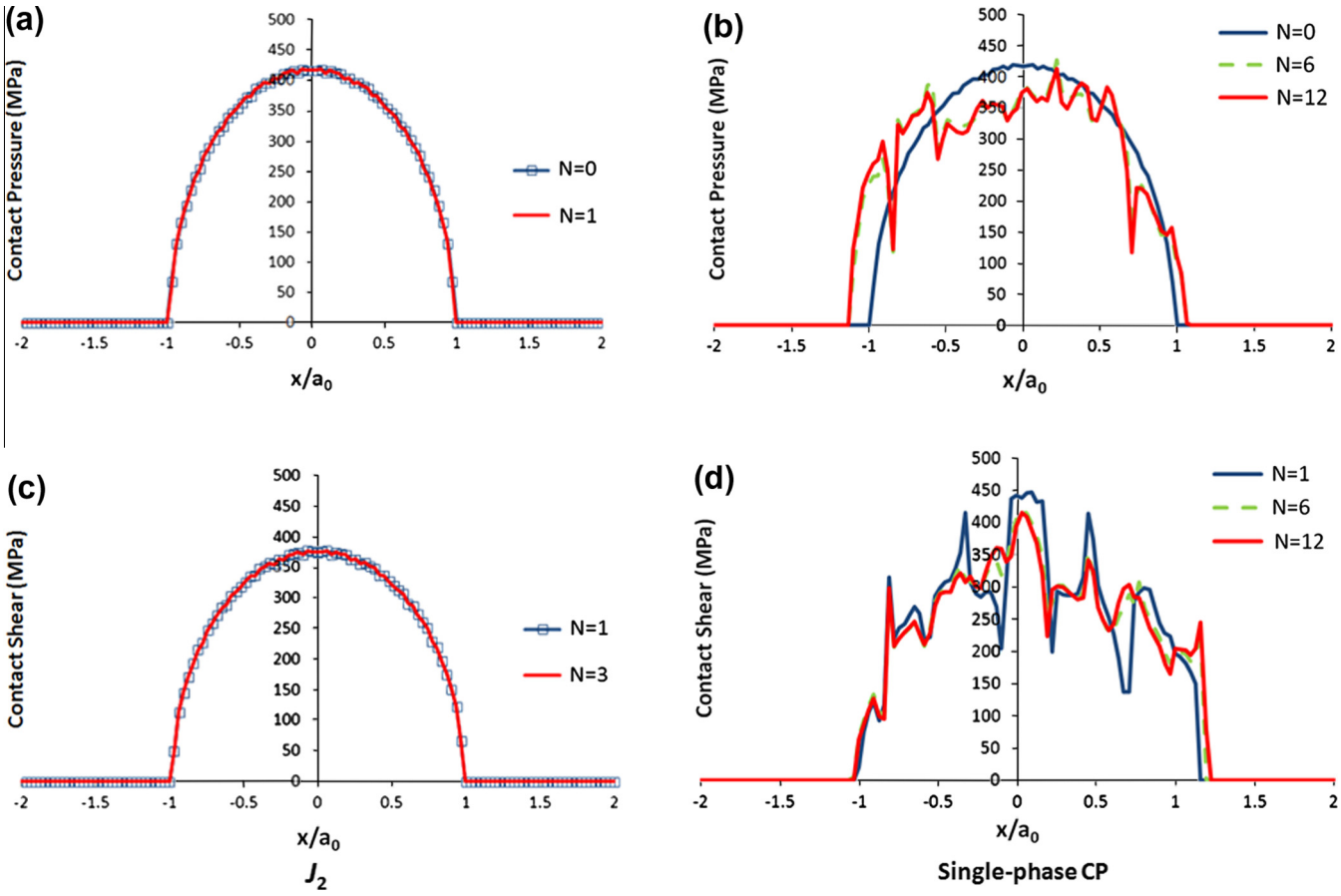

Fig. 12. Evolutions of predicted contact variable distributions for J_2 and single phase CP model under gross slip conditions $P = 50$ N/mm and $\delta_{app} = 50$ μm.

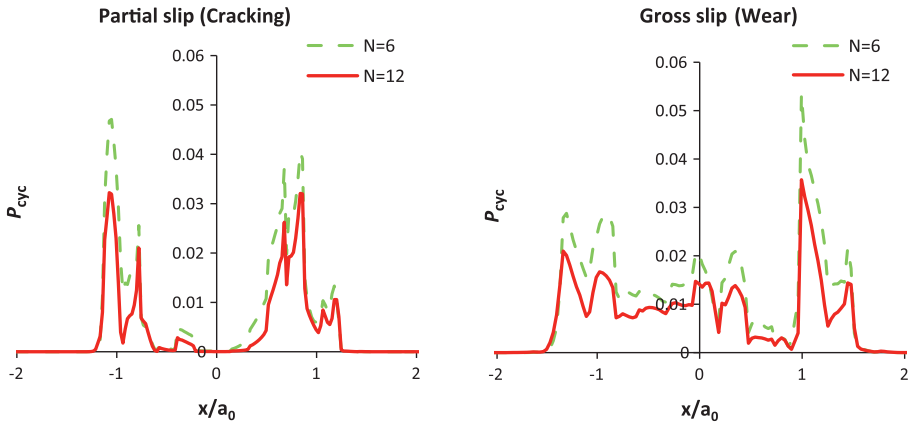

(a) CP model, $\delta_{app} = 100$ μm, $P = 100$ N/mm (b) CP model, $\delta_{app} = 80$ μm, $P = 50$ N/mm

Fig. 13. Predicted evolution of accumulated plastic slip per cycle, p_{cyc}, for two different fretting regimes.

Table 5
p_{crit} Based fretting micro-crack initiation predictions.

p_{crit}	Partial slip	Gross slip
No. of cycles, N_i	1609	1452

mentioned above, are indicative of the development of "natural surface roughness" [14]. An apparent stick region is observed in Fig. 16 showing the distribution of the contact slip for the 12th cycle for a typical partial slip situation. However on closer inspection the "stick–slip interface" is not at a single point but is distributed over a region where both sticking and slipping are predicted. This region is a typical location for cracking to occur, as can be seen from the SEM image shown in Fig. 17a. It can also be seen that cracking is not limited solely to the stick–slip interface but can occur anywhere within the slip zone. Table 6 also shows the predicted crack locations for the five random orientation sets, in comparison with the corresponding experimental crack location range. Comparing the CP model in Fig. 17b to the SEM image of

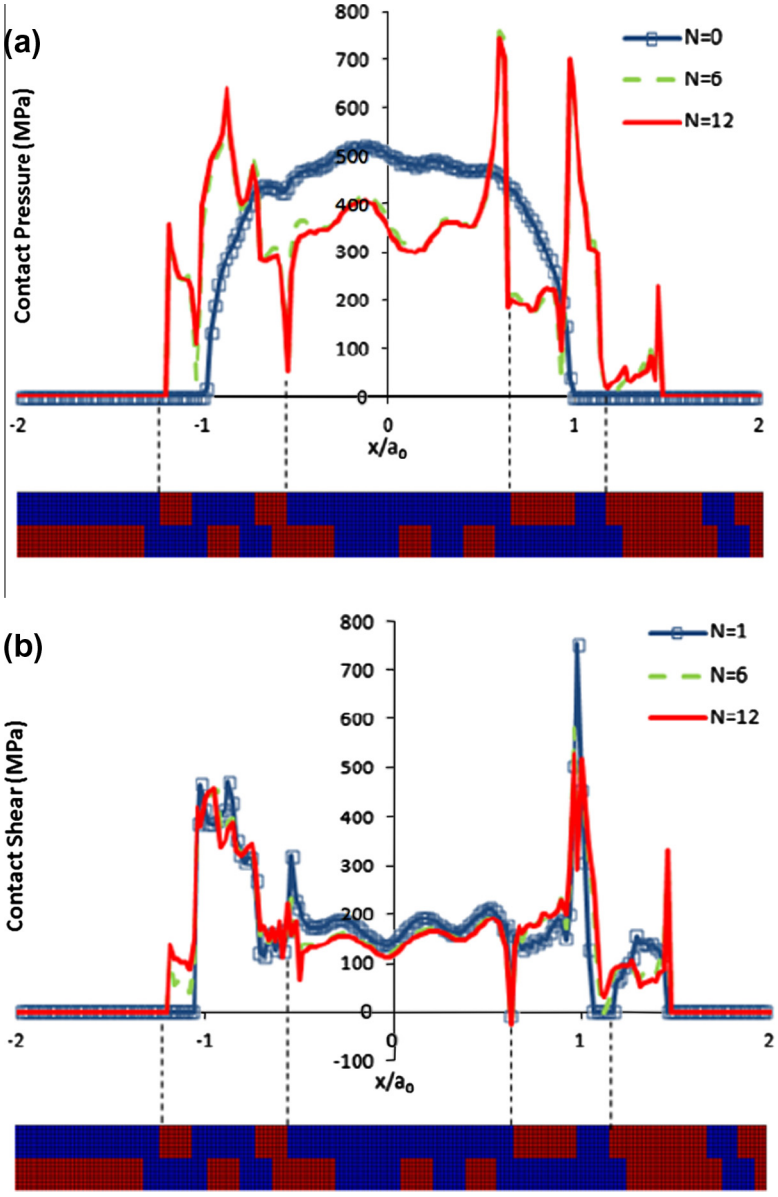

Fig. 14. Dual phase CP model contact variables with the top layer of the Ti–6Al–4V microstructure highlighting the effect of phase boundary interface on stress heterogeneity (partial slip case).

crack initiation sites in Fig. 17a [8] we can see correlation in terms of micro-crack location. These comparisons are taken after 300,000 cycles for a partial slip situation.

3.5. Wear scar predictions and wear coefficients

Applying the microstructure-sensitive fretting wear extrapolation technique of Fig. 6, wear scars are predicted for the distributions of p_{cyc} presented for the gross slip CP model in Fig. 18. Damage is predicted across the entire contact region, corresponding to Case B (Wear) of Fig. 5, and resulting in a "U shaped" wear scar. Fig. 18 and Table 7 compare the experimentally measured wear scar to the FE predicted wear profile after 100,000 cycles. An Archard wear coefficient is computed from the predicted wear scar using the equation:

$$k = \frac{V}{PS} \tag{14}$$

where k is the wear coefficient, V is the measured wear volume, P the normal load and S is the total sliding distance. Using the wear scar presented in Fig. 19 a comparison is given in Table 8 between the measured experimental and FE predicted wear coefficient after 300,000 cycles.

4. Discussion

The accumulated plastic slip per cycle parameter, p_{cyc}, presented in Fig. 13, gives distinct differences between the two sliding regimes. While the predicted crack initiation lives are similar, the form of p_{cyc} distribution, allows differentiation between the resulting modes of fretting damage. For Case A (cracking), localised peaks in p_{cyc}, and hence micro-cracking, are predicted across the contacting surfaces and, therefore, this will lead to localised crack propagation and premature failure, upon fatigue loading of the substrate. In contrast, Case B (wear) predicts a more uniform micro-cracking and micro-damage occurring across the entire contact

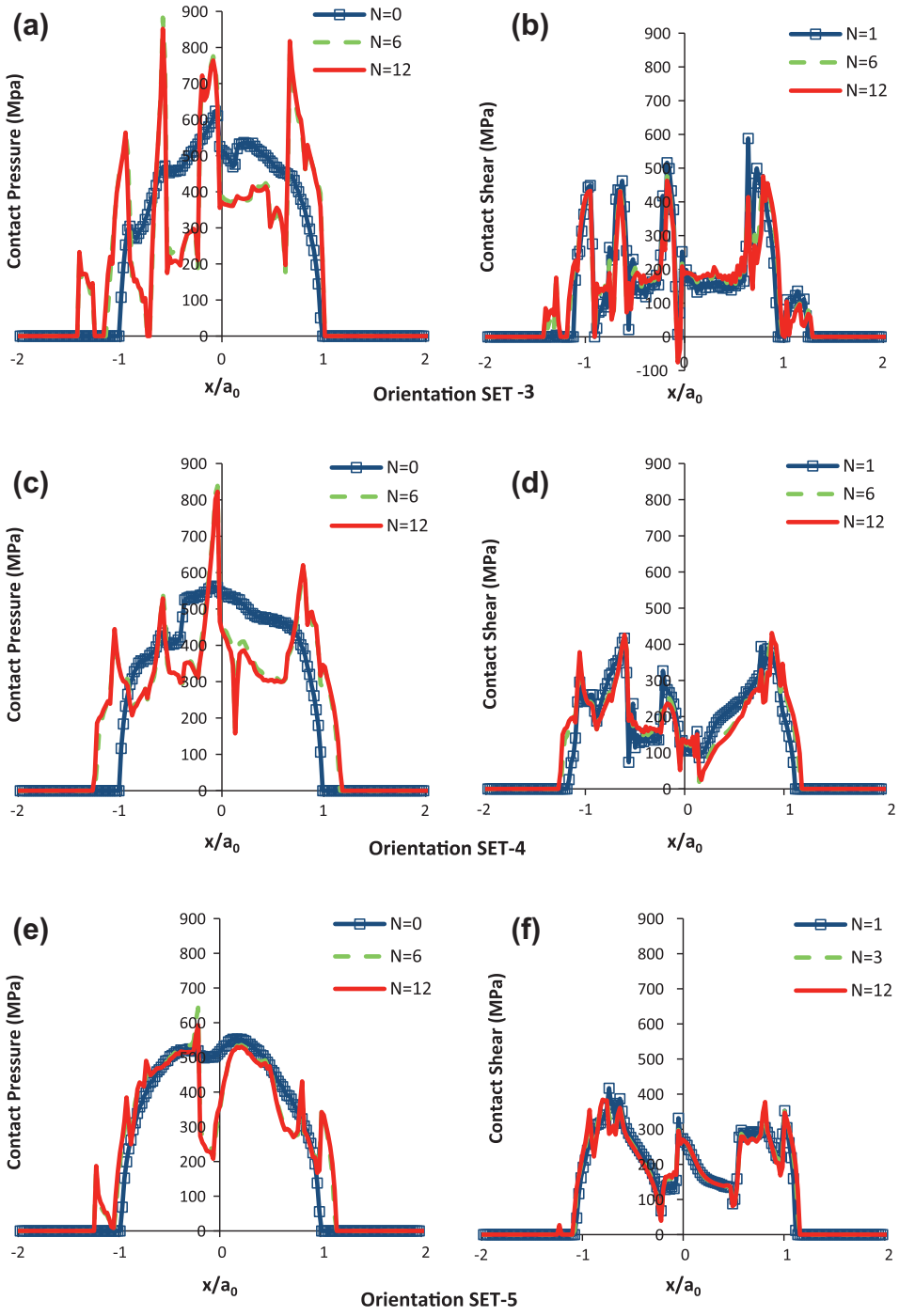

Fig. 15. The effect of random orientation on contact variables (pressure and shear) for the dual phase microstructure for a sample of three different orientation sets of Table 6: (a and b) for orientation set 3; (c and d) for orientation set 4 and (e and f) for orientation set 5.

Table 6
Comparisons between experimental and CP (dual phase model) predicted crack initiation, crack orientations and crack locations.

Orientation	Crack angle (°)	Location (x/a_0)	N_i
Experimental	<30	0.4–0.9	$<1 \times 10^5$
Predicted			
SET-1	6	0.65	3.1×10^3
SET-2	21	0.67	3.2×10^3
SET-3	30	1.24	2.2×10^3
SET-4	3	0.02	1.1×10^4
SET-5	29	1.1	7.1×10^3
Average	17.8	0.736	5.2×10^3

region. This uniform micro-cracking process will inevitably lead to asperity removal, debris, stress redistribution and eventually wear. This form of fretting damage will result in an increase in number of cycles to fatigue failure compared to the partial slip regime, in situations involving substrate fatigue loading [3].

Considerable phase boundary effects are evident from the contact variable distributions of the dual phase CP model that were not captured by the single phase CP model (Figs. 14 and 15). These effects are due to the variations in yield stresses between the "harder" α phase and "softer" α–β phase grains. The effect of random orientation is investigated for the partial slip

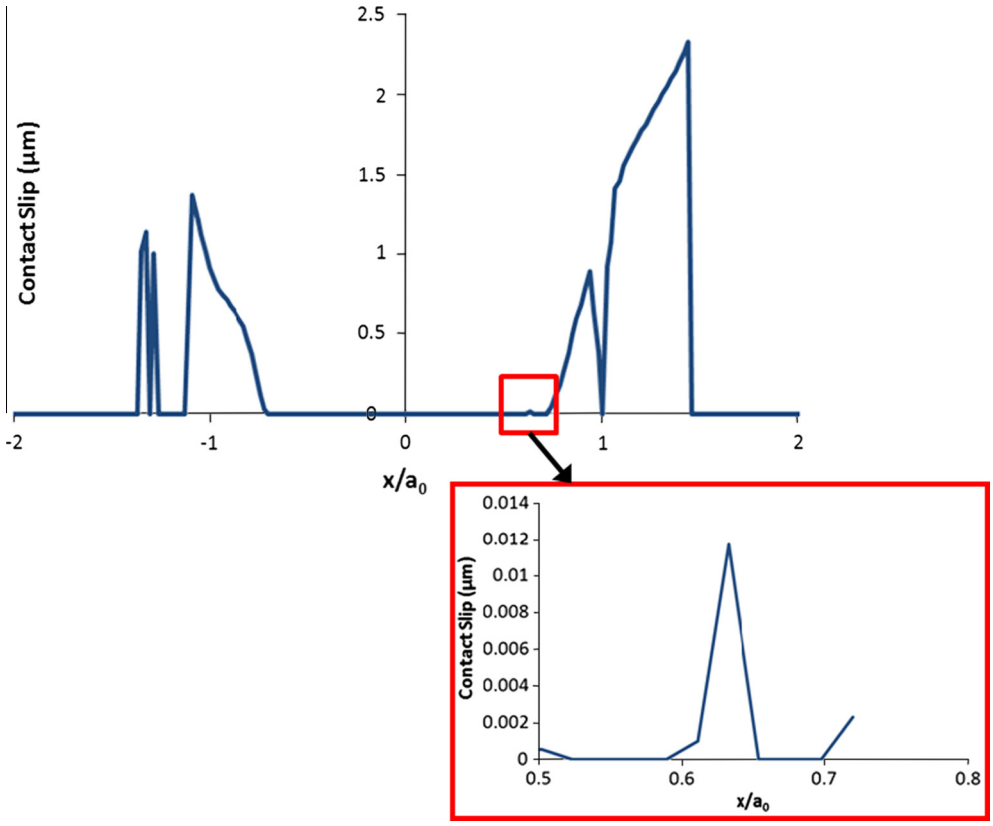

Fig. 16. Contact slip distribution for 12th cycle highlighting the occurrence of a " natural surface roughness " within the CP model as a result of the varying yield stress of individual grains.

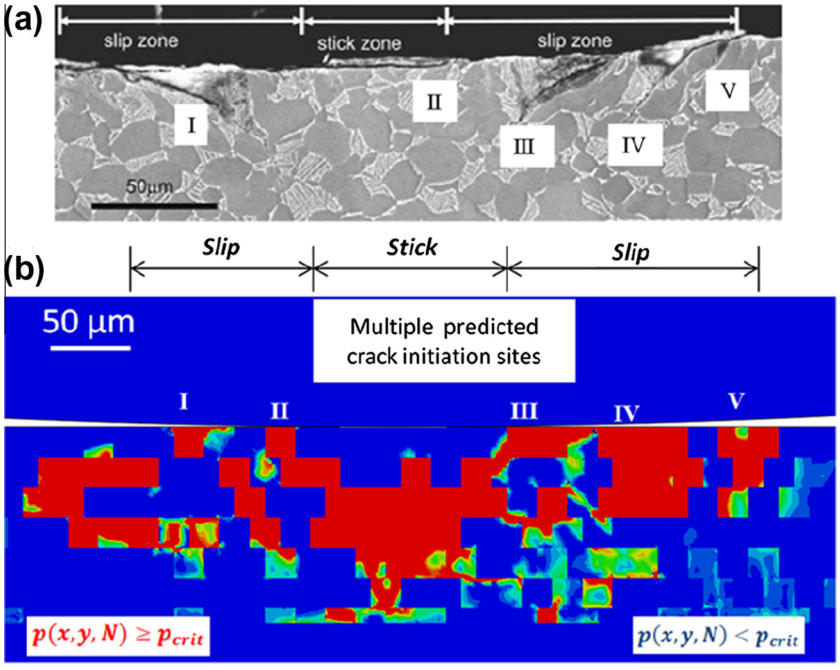

Fig. 17. (a) SEM image of a partial slip case after 300,000 cycles [8], and (b) p_{cyc} based crack prediction for partial slip case after 300,000 cycles.

model to compare against the experimental results. The CP model can capture fatigue scatter as illustrated in Figs. 9 and 10. This benefit is further evident in Table 6 where different initiation lives are predicted based on random orientation effects. Ding et al. [8] observed crack nucleation lengths from 5 to 50 µm and stated that all cracks nucleated within 10^5 cycles. The hybrid CP model predicts cracks nucleating at length scales less than 2.5 µm and predicts initiation lives that compare well with the experimental data, given the shorter length-scales of the CP-predicted "cracks".

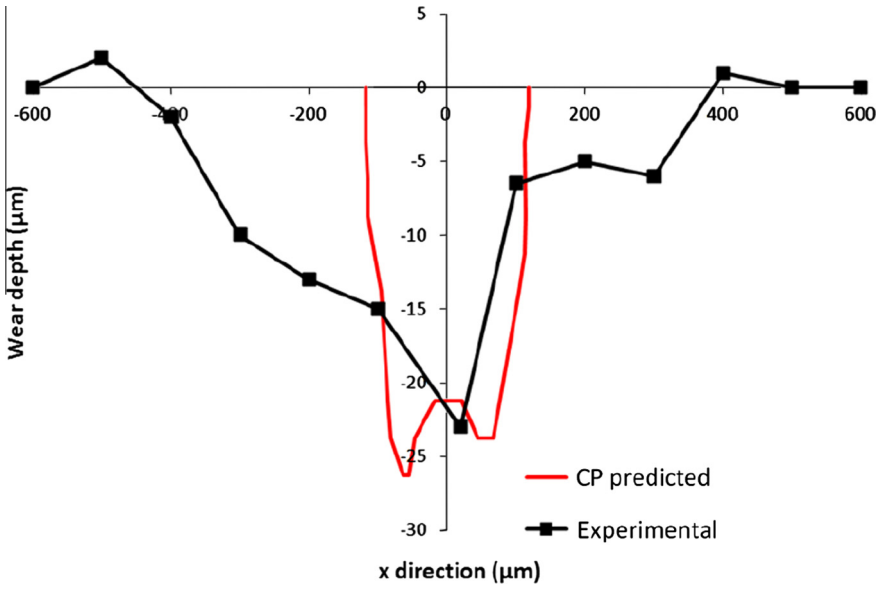

Fig. 18. Comparison of the FE predicted and the experimentally measured [8] wear profile for gross sliding (P = 50 N/mm, δ_{app} = 80 μm) after 100,000 cycles.

Table 7
Comparison of wear scar dimensions for the measured experimental and FE predicted wear profile after 100,000 cycles.

	Maximum wear depth (μm)	Wear scar width (μm)
Experimental	23	1100
Predicted	26	237

Using the dual phase CP model, reasonable correlation is evident for predicting crack locations throughout the contact region. The p_{cyc} distribution of Fig. 17b can be compared against the SEM image (Fig. 17a) after 300,000 cycles. Cracks are shown to occur not only at the trailing edge of contact or the stick–slip interface, as conventional FIP's predict [8], but throughout the slip zone, depending on microstructural effects or deformities. The dual phase CP model has the ability to model these microstructural effects and highlights similar cracking locations (Table 6). These crack locations are heavily influenced by the position of phase boundaries and favourably orientated grains. Although the majority of crack initiation sites correlate with the experimental results, orientation SET-4 predicts a nucleation site at the contact centre. While this is an unusual location for cracking under partial slip conditions, it corresponds to a phase boundary, coinciding with a favourably orientated grain, which causes a significant build-up in crystallographic slip. The strong mismatch between α and α–β phase properties, coupled with the high coefficient of friction, results in significant predicted discontinuities of contact pressure, shear (Figs. 14 and 15) and associated subsurface stresses and crys-

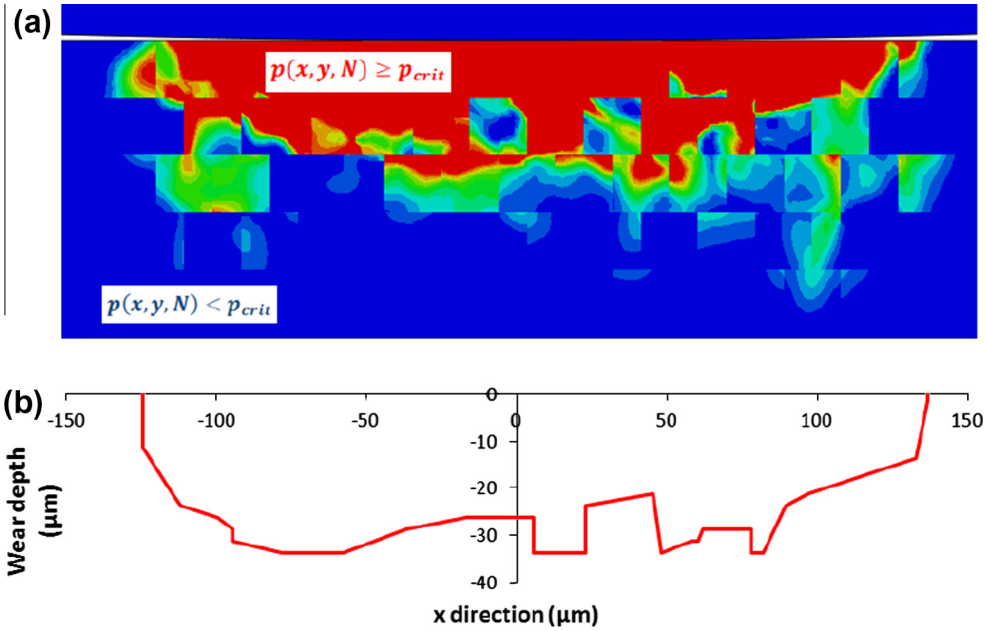

Fig. 19. Extrapolated wear scar after 300,000 cycles: (a) smoothed wear scar of $p(x, y, N)$ and (b) calculated wear profile, for gross sliding (P = 50 N/mm, δ_{app} = 80 μm) using p_{cyc}.

Table 8
Comparison between the measured experimental and the FE predicted wear coefficient after 300,000 cycles for the gross slip case.

	Wear coefficient (MPa^{-1})
Experimental	8.2×10^{-9}
Predicted	2.89×10^{-9}

tallographic slips. This in turn has led to convergence difficulties for the gross slip (wear) analyses; hence, the gross slip analyses in the present work employ the single phase CP material model.

The FE predicted gross slip wear scar (Fig. 18) gives good correlation with the experimental for maximum wear depth; however the predicted width is significantly less than the measured width. The wear methodology presented here does not include material removal, e.g. Madge et al. [3], or wear debris effects, e.g. Ding et al. [29]. After 100,000 cycles there is significant widening of the experimental contact zone as a result of material removal, debris and ploughing effects. It is also important to note that the FE model is a two-dimensional representation of a 3D fretting wear scar sampled along a particular transverse location across the specimen width. Sampling along different transverse locations could be expected to result in, at least slightly, different experimental wear scar profiles. This type of effect requires three-dimensional CP modelling.

The good correlation of predicted wear coefficient, of approximately $3 \times 10^{-9}\,MPa^{-1}$, with the experimental value of approximately $8 \times 10^{-9}\,MPa^{-1}$, gives confidence in the ability of CP modelling to capture the important effects of micro-plasticity, and hence micro-fatigue, in the wear process for Ti–6Al–4V. A key next step is the development of a material removal wear simulation methodology based on the use of p_{cyc}, instead of the Archard or energy based [3,30] wear methods. This would give a more scale-consistent, and hence fundamental approach, which could also achieve unification of crack initiation for fatigue and wear.

This paper has assumed a regular microstructure (grain shape and size). Clearly, the real microstructure has a statistical distribution of grain size and grain shape, which in turn affects microcracking (wear) and fretting crack nucleation. Of course, texture can have an important role on fretting behaviour. The work of Goh et al. [31], for example, highlights a considerable effect of texture on plastic strain accumulation and states that the role of texture may be significant in resisting fretting damage. The experimental work of Ding et al. [8] however indicated no significant texture within the material tested here. Since grain size has a significant effect on fatigue crack initiation and propagation [32], length scale effects (viz. strain gradient plasticity [33]), also need to be incorporated into future CP modelling.

5. Conclusion

A microstructure-sensitive crack initiation predictive methodology was implemented for fretting of Ti–6Al–4V. Significant effects of micro-plasticity on the evolutions of fretting contact tractions are demonstrated for an ostensibly elastic fretting loading situation. The microstructure-sensitive approach (i) predicted partial slip cracking (multiple sites, number of cycles to crack initiation, crack angles and crack locations), corresponding with experimental data, and (ii) was adopted to facilitate a novel wear prediction methodology, which predicted a wear coefficient and a two-dimensional wear scar reasonably consistent with experimental data for gross slip cases.

Acknowledgement

SFI/HEA Irish Centre for High-End Computing (ICHEC) for the provision of computational facilities and support.

References

[1] Ding J, Houghton D, Williams EJ, Leen SB. Simple parameters to predict effect of surface damage on fretting fatigue. Int J Fatigue 2011;33(3):332–42.
[2] Vingsbo O, Soderberg D. On fretting maps. Wear 1988;126:131–47.
[3] Madge JJ, Leen SB, McColl IR, Shipway PH. Contact-evolution based prediction of fretting fatigue life: effect of slip amplitude. Wear 2007;262(9–10):1159–70.
[4] Madge JJ, Leen SB, Shipway PH. The critical role of fretting wear in the analysis of fretting fatigue. Wear 2007;263(1–6):542–51.
[5] Archard JF. Contact and rubbing of flat surfaces. J Appl Phys 1953;24(8):981–8.
[6] Hutchings IM. Tribology: friction and wear of engineering materials. Oxford: Butterworth-Heinemann; 1992.
[7] McDowell DL, Dunne FPE. Microstructure-sensitive computational modeling of fatigue crack formation. Int J Fatigue 2010;32(9):1521–42.
[8] Ding J, Bandak G, Leen SB, Williams EJ, Shipway PH. Experimental characterisation and numerical simulation of contact evolution effect on fretting crack nucleation for Ti–6Al–4V. Tribol Int 2009;42(11–12):1651–62.
[9] Madge JJ, Leen SB, Shipway PH. A combined wear and crack nucleation–propagation methodology for fretting fatigue prediction. Int J Fatigue 2008;30(9):1509–28.
[10] McHugh PE, Connolly PJ. Micromechanical modelling of ductile crack growth in the binder phase of WC–Co. Comput Mater Sci 2003;27(4):423–36.
[11] McGarry JP, O'Donnell BP, McHugh PE, O'Cearbhaill E. Computational examination of the effect of material inhomogeneity on the necking of stent struts under tensile loading. J Appl Mech 2007;74:978–90.
[12] Mayeur JR, McDowell DL, Neu RW. Crystal plasticity simulations of fretting of Ti–6Al–4V in partial slip regime considering effects of texture. Comput Mater Sci 2008;41(3):356–65.
[13] Zhang M, Neu RW, McDowell DL. Microstructure-sensitive modeling: application to fretting contacts. Int J Fatigue 2009;31(8–9):1397–406.
[14] Goh C-H, McDowell DL, Neu RW. Plasticity in polycrystalline fretting fatigue contacts. J Mech Phys Solids 2006;54(2):340–67.
[15] Manonukul A, Dunne FPE. High and low cycle fatigue crack initiation using polycrystal plasticity. Proc R Soc 2004;460:1881–903.
[16] McCarthy OJ, McGarry JP, Leen SB. A finite element study of microstructure-sensitive plasticity and crack nucleation in fretting. Comput Mater Sci 2011;50(8):2439–58.
[17] Dick T, Cailletaud G. Fretting modelling with a crystal plasticity model of Ti6Al4V. Comput Mater Sci 2006;38(1):113–25.
[18] Dick T, Basseville S, Cailletaud G. Fatigue modelling in fretting contact with a crystal plasticity model. Comput Mater Sci 2008;43(1):36–42.
[19] Benedetti M, Fontanari V. The effect of bi-modal and lamellar microstructures of Ti–6Al–4V on the behaviour of fatigue cracks emanating from edge-notches. Fatigue Fract Eng Mater Struct 2004;27(11):1073–89.
[20] Hasija V, Ghosh S, Mills MJ, Joseph DS. Deformation and creep modeling in polycrystalline Ti–6Al alloys. Acta Mater 2003;51(15):4533–49.
[21] Khan AS, Huang S. Continuum theory of plasticity. John Wiley & Sons; 1995.
[22] D. Peirce, R.J. Asaro, A. Needleman, Material rate dependence and localized deformation in crystalline solids. Acta Metallurgica 1983;31(12):1951–1976.
[23] Bache MR, Dunne FPE. Experimental and crystal plasticity studies of deformation and crack nucleation in a titanium alloy. J Strain Anal Eng Des 2010;45(5):391–9.
[24] Morrissey RJ, McDowell DL, Nicholas T. Microplasticity in HCF of Ti–6Al–4V. Int J Fatigue 2001;23(Supplement 1):55–64.
[25] McColl IR, Ding J, Leen SB. Finite element simulation and experimental validation of fretting wear. Wear 2004;256(11–12):1114–27.
[26] Jin O, Mall S. Effects of slip on fretting behavior: experiments and analyses. Wear 2004;256(7–8):671–84.
[27] Johnson KJ. Contact mechanics. Netherlands: Cambridge University Press; 1985.
[28] Sweeney CA, McHugh PE, McGarry JP, Leen SB. Micromechanical methodology for fatigue in cardiovascular stents. Int J Fatigue 2012;44:202–16.
[29] Ding J, McColl IR, Leen SB, Shipway PH. A finite element based approach to simulating the effects of debris on fretting wear. Wear 2007;263(1–6):481–91.
[30] Zhang T, McHugh PE, Leen SB. Computational study on the effect of contact geometry on fretting behaviour. Wear 2011;271(9–10):1462–80.
[31] Goh C-H, Wallace JM, Neu RW, McDowell DL. Polycrystal plasticity simulations of fretting fatigue. Int J Fatigue 2001;23(Supplement 1):423–35.
[32] Miller KN. Materials science perspective of metal fatigue resistance. Mater Sci Technol 1993;9:453.
[33] Dunne FPE, Rugg D, Walker A. Lengthscale-dependent, elastically anisotropic, physically-based hcp crystal plasticity: application to cold-dwell fatigue in Ti alloys. Int J Plast 2007;23(6):1061–83.